Available online at www.sciencedirect.com
ScienceDirect
Trans. Nonferrous Met. Soc. China 32(2022) 2838−2851
Transactions of Nonferrous Metals Society of China
www.tnmsc.cn

Effect of aging time on discontinuous precipitates, continuous precipitates and mechanical properties of AZ80A magnesium alloy

Ke-long ZHANG[1], Hui-zhong LI[1,2,3], Xiao-peng LIANG[1,2,3], Zhi CHEN[1], Zi-xuan ZHAO[1], Hui TAO[1], Xiong-wen ZHOU[4]

1. School of Materials Science and Engineering, Central South University, Changsha 410083, China;
2. State Key Laboratory of Powder Metallurgy, Central South University, Changsha 410083, China;
3. Key Laboratory of Nonferrous Metal Materials Science and Engineering, Ministry of Education, Central South University, Changsha 410083, China;
4. Department of Prosthodontics, Center of Stomatology, Xiangya Hospital, Central South University, Changsha 410008, China

Received 17 August 2021; accepted 8 March 2022

Abstract: The evolution of precipitates and mechanical properties of AZ80A magnesium alloy with aging time was studied by in situ observation with SEM, TEM and tensile testing. The results show that the continuous precipitation (CP) phases near the reaction front (RF) are replaced by the discontinuous precipitation (DP) phases at the early aging stage. In DP regions, the elliptical phases coarsen obviously with the increase of aging time, which results in a slightly slow reduction of the intracrystalline hardness of DP regions. In CP regions, some small plate phases reprecipitate simultaneously with the growth of the initial precipitates, which contributes to a slight increase in the intracrystalline hardness in CP regions at the later aging stage. The aging hardening of DP regions is faster and stronger than that of CP regions. However, the age strengthening of CP regions not only compensates for the overaging softening of DP regions but also improves the strength of the alloy.

Key words: age hardening; discontinuous precipitation; coarsening; in situ observation; mechanical properties; magnesium alloy

1 Introduction

Magnesium alloys are becoming increasingly attractive in the transportation industry due to their low density [1], good vibrational absorption [2], high stiffness [3] and specific strength [4]. For example, the Boeing 727 aircraft contains approximately 1200 magnesium parts [5]. The engine block, cylinder head covers and many other parts are made of magnesium alloys in the automotive sector [6]. Compared with other magnesium alloys, Mg−Al series magnesium alloys are more commonly used because of their excellent hot working performance [7], outstanding fracture toughness [8] and relatively low cost [9]. For instance, an AJ62 alloy engine block is used by BMW [10]. AZ31 alloy brackets and AZ80 alloy car wheel rims were reported in Ref. [11]. However, for further applications, there is an urgent need to improve its mechanical properties, especially the strength.

As heat-treatable strengthening alloys, Mg−Al series alloys, such as AZ31 [12], AZ61 [13], AZ80 [14] and AZ91 [15], are strengthened by the β-$Mg_{17}Al_{12}$ phase, which is normally precipitated

Corresponding author: Xiao-peng LIANG, Tel: +86-18684894344, E-mail: liangxp@csu.edu.cn;
Xiong-wen ZHOU, Tel: +86-13707310367, E-mail: zhouxw1128@163.com
DOI: 10.1016/S1003-6326(22)65987-9

by continuous precipitation (CP) and discontinuous precipitation (DP) during aging [16]. CP produces a substantial number of Widmanstätten phases, which are asymmetricly lozenge-shaped plate phases [17], while DP creates a large number of lamellar phases and elliptical phases, accompanied by a small number of intergranular phases [18]. Many studies show that both CP and DP have an impact on the age hardening response of Mg−Al series alloys [19−21]. CELOTTO [20] reported that the hardness increases when asymmetricly lozenge-shaped precipitates extend into long laths along the basal plane and reach the peak hardness with the maximum length of the lath. The effect of CP was discussed here, but that of DP was neglected. Some researchers found that the hardness of AZ92 alloy increases as DP is promoted when the alloy is aged at 200 °C [21]. Here, DP has a great impact on the age hardening response. In our previous study [14], it was revealed that the age hardening effect of DP is better than that of CP when the alloy is peak-aged between 150 and 200 °C. However, the age hardening behavior and the microstructure evolution of DP regions have rarely been studied together with those of CP regions. Because CP and DP proceed separately and competitively during the aging process [22], their age hardening behavior, especially for their peak aged point, may be different. Moreover, the development of different kinds of precipitates with various morphologies may also differ from one another. The result of competition is critical to the age hardening response of the alloy. Thus, synthetic analysis of the age hardening behavior and microstructural evolution of the CP and DP regions has directive significance for controlling the proportions of CP and DP in the aged alloy and improving the performance of Mg−Al series magnesium alloys.

The present research aimed to study the age hardening behavior of CP and DP regions by testing their intracrystalline microhardness, and analyze their microstructure variation over aging time by optical microscopy, scanning electron microscopy and transmission electron microscopy. The relationship between the microstructure and intracrystalline microhardness of the CP and DP regions, as well as their contribution to the mechanical properties of the alloy, were also discussed.

2 Experimental

The material employed in the present work was an AZ80A magnesium alloy with chemical composition (wt.%) of 8.06 Al, 0.62 Zn, 0.23 Mn, and balanced Mg. The as-received material was a forged billet with a diameter of 730 mm and a length of 110 mm. The forged billet was obtained after 3 passes of forging on a semi-continuous ingot with a diameter of 300 mm and a length of 650 mm. Before forging, casting ingots were homogenized at 410 °C for 24 h. Specimens for the hardness test with a size of 8 mm × 10 mm × 2 mm were cut from the forged billet, and specimens for the tensile test were fabricated to a gauge length of 25 mm, a gauge width of 10 mm and a thickness of 2 mm. Then, those specimens were solid solution treated at 420 °C for 2 h, followed by water cooling and subsequent aging at 175 °C for different time.

Tensile experiments were carried out on an MTS810 tensile test machine. Hardness was tested on an HVS 1000S Vickers hardness machine with a load of 4.98 N and loading time of 15 s. For intracrystalline hardness tests, 100 points were tested under a load of 0.245 N. The ordinal number of the point and the corresponding hardness values were recorded first, and then those located at the grain boundaries were discarded and those in the CP or DP regions were classified by optical microscopy. Finally, both the average hardness values of CP and DP regions were obtained.

Optical microscopy (OM), scanning electron microscopy (SEM, SIRION200) and transmission electron microscopy (TEM, Tecnai G2 20 ST, 200 kV) were used to investigate the microstructures. Specimens for in situ SEM observation were mechanically polished and marked with a Vickers hardness machine at the beginning. Then, they were solid solution treated and aged at 175 °C. Before the first SEM observation, the specimens were electrolytically polished. After further aging, the specimens were lightly mechanically polished again to remove the oxide layer. Finally, they were etched with a solution composed of 0.5 vol.% nitric acid and 99.5 vol.% alcohol before the second SEM observation. Other samples for OM and SEM observation were etched with the same solution. Thin foils for TEM observation were prepared by the ion beam thinning technique. The fractions of

DP and CP regions were calculated with IPP (Image-Pro Plus) software from at least 5 OM pictures.

3 Results

3.1 Age hardening behavior

The effect of aging time on hardness and fraction of DP regions of the AZ80A magnesium alloy aged at 175 °C is shown in Fig. 1. At the beginning of aging, the hardness of the alloy increases rapidly. After 28 h, it continues to grow at a decreasing rate and reaches a peak value of HV 85.9 at 106 h. During the following aging time, even after 328 h, the alloy does not show any obvious overaging characteristics. Meanwhile, Fig. 1 also shows the variation in the fraction of DP regions with a similar pattern over aging time. The fraction of DP regions increases quickly at first and then stops increasing when it reaches the maximum value at 53 h. This implies that DP regions play an important role in age hardening behavior with respect to microstructure.

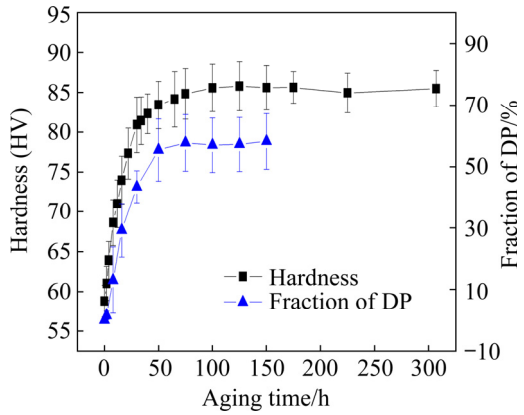

Fig. 1 Age hardening behavior of AZ80A magnesium alloy aged at 175 °C

3.2 Microstructures

The optical microstructures of the AZ80A magnesium alloys aged at 175 °C for different time are shown in Fig. 2. The average grain size of the solution heat-treated alloy is approximately 80 μm, as shown in Fig. 2(a). Figure 2(b) shows that DP regions appear at the original grain boundaries (OGB) at the beginning of aging. DP regions grow and extend into the grain interior (original matrix/CP region) with increasing aging time, as shown in Figs. 2(b−d). However, the size of DP regions has no obvious change with increasing aging time from 53 to 328 h, as shown in Figs. 2(d−f), suggesting that DP regions have stopped growing since 53 h. The development of DP regions is clearly seen in the OM microstructure, but many details of DP and CP cannot be well observed. To understand the age hardening behavior of the CP and DP regions, SEM and TEM microstructure investigations were performed.

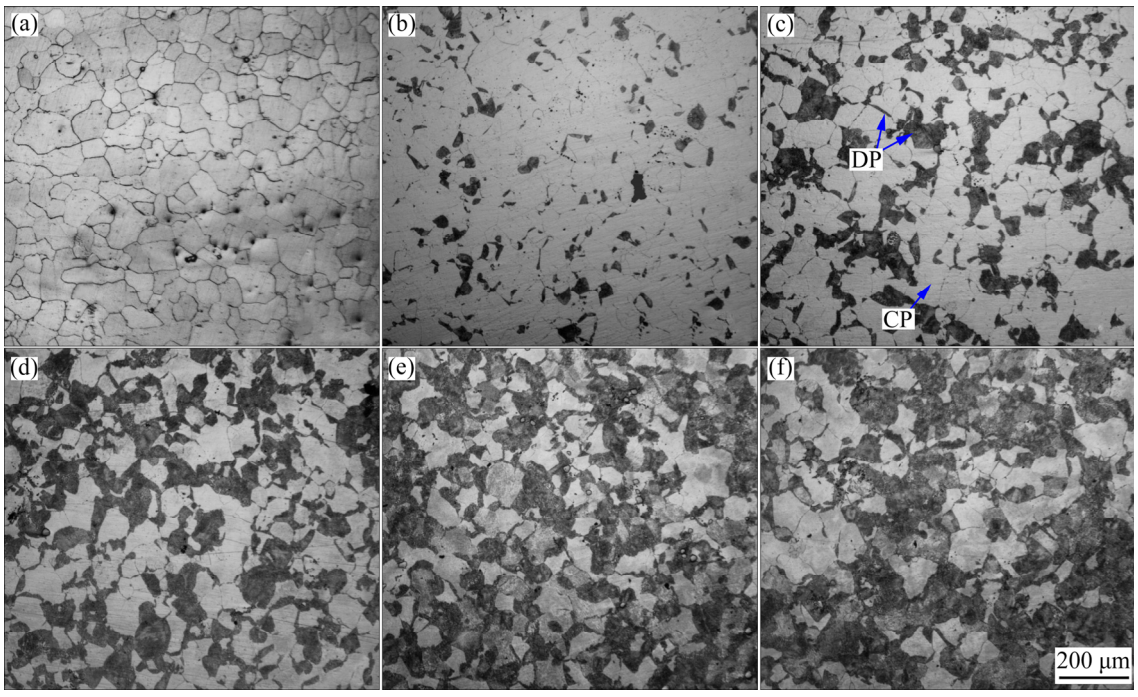

Fig. 2 OM images of alloy aged at 175 °C for different time: (a) 0 h; (b) 6 h; (c) 28 h; (d) 53 h; (e) 106 h; (f) 328 h

3.2.1 Microstructures at beginning of aging

Figures 3(a) and (b) show the SEM microstructures of the alloy aged for 6 h. Small cellular structures, a typical structure of DP, originate from the grain boundaries. They grow either on one side to form a so-called “single seam” morphology or develop alternately on both sides of the boundary in an “S” morphology [23], as shown in Figs. 3(a) and (b), respectively.

Figures 3(c−e) show the TEM microstructures of the alloy aged for 6 h. At the beginning of aging, precipitates nucleate in the grain interior/original matrix and at original grain boundary (OGB). Small precipitates in the grain interior exhibit a lozenge shape in view of the $[0001]_m$ zone axis, which are typical Widmanstätten structures of CP, as shown in Fig. 3(c). However, the intergranular phases at the OGB, which belong to DP precipitates [17], are much larger than those in the grain interior, as shown in Fig. 3(d). Accompanied by the growth of precipitates, the OGB bends into the matrix of grains on both sides, leading to an “S”-shaped grain boundary, as shown in Fig. 3(e). As a result, two small cellular structures form on the two sides. This is known as the “S” type nucleation of DP [18]. Here, the migrating OGB acts as a reaction front (RF) of cellular structures [23]. The intergranular phases are left at the position where the OGB stays before and makes up a stationary boundary between CP regions and cellular structures. It is called static boundary (SB) in this article. Both RF and SB are the boundaries of cellular structures.

3.2.2 Variation of microstructures in DP regions

The SEM images of the alloys aged for different time are shown in Fig. 4. When the alloy is aged from 28 to 53 h, in situ observation reveals that the RF at 28 h (RF28) migrates toward the original matrix region/CP region and reaches the position of RF53, as shown in Figs. 4(a) and (b). The small precipitates that have already formed in CP regions between RF28 and RF53 disappear and are replaced by elliptical phases or lamellar phases. As a result, the cellular structure grows up. When the alloy is further aged from 53 to 78 h, RF53 almost overlaps with RF78, as shown in Figs. 4(c) and (d), indicating that the RF stops migrating at 53 h.

After 53 h, the cellular structure no longer grows because the RF stops migrating, while the situation of the precipitates in DP regions is different. The precipitates at OGBs and SBs (marked with blue arrows) are mainly granular, also

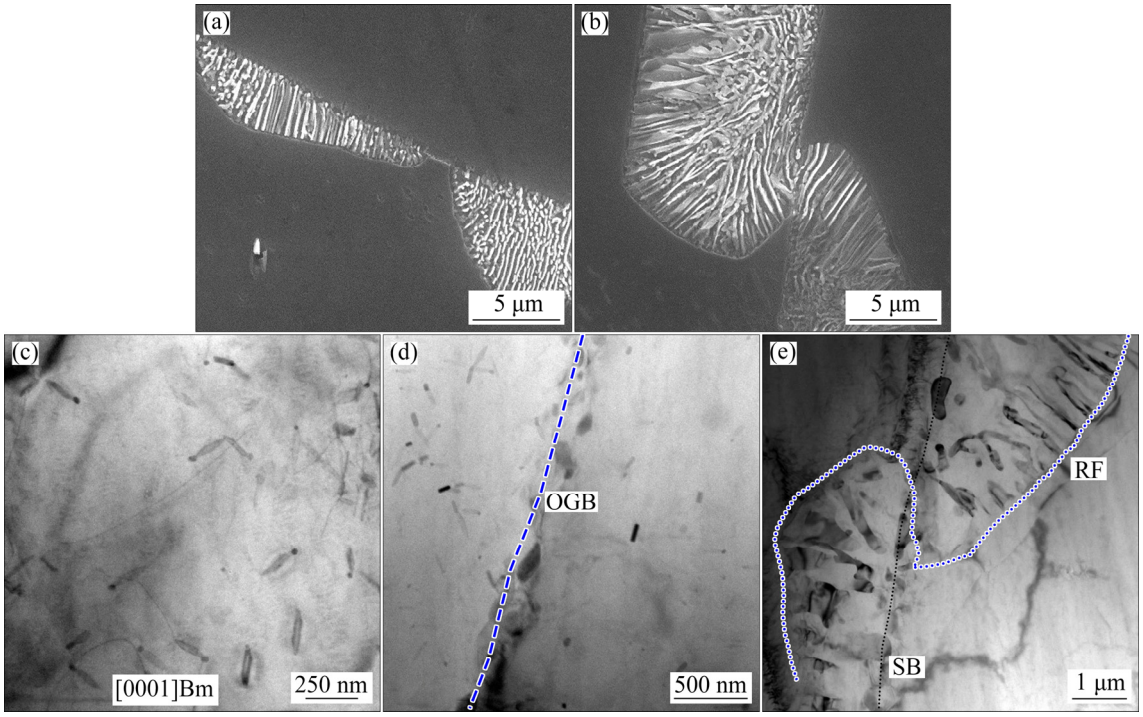

Fig. 3 SEM (a, b) and TEM (c−e) images of precipitates in AZ80A magnesium alloy aged for 6 h: (a, b, e) Small cellular structure with single seam morphology (a) and “S”-shaped morphology (b, e); (c) Small lozenge shape plate phases; (d) Intergranular phase

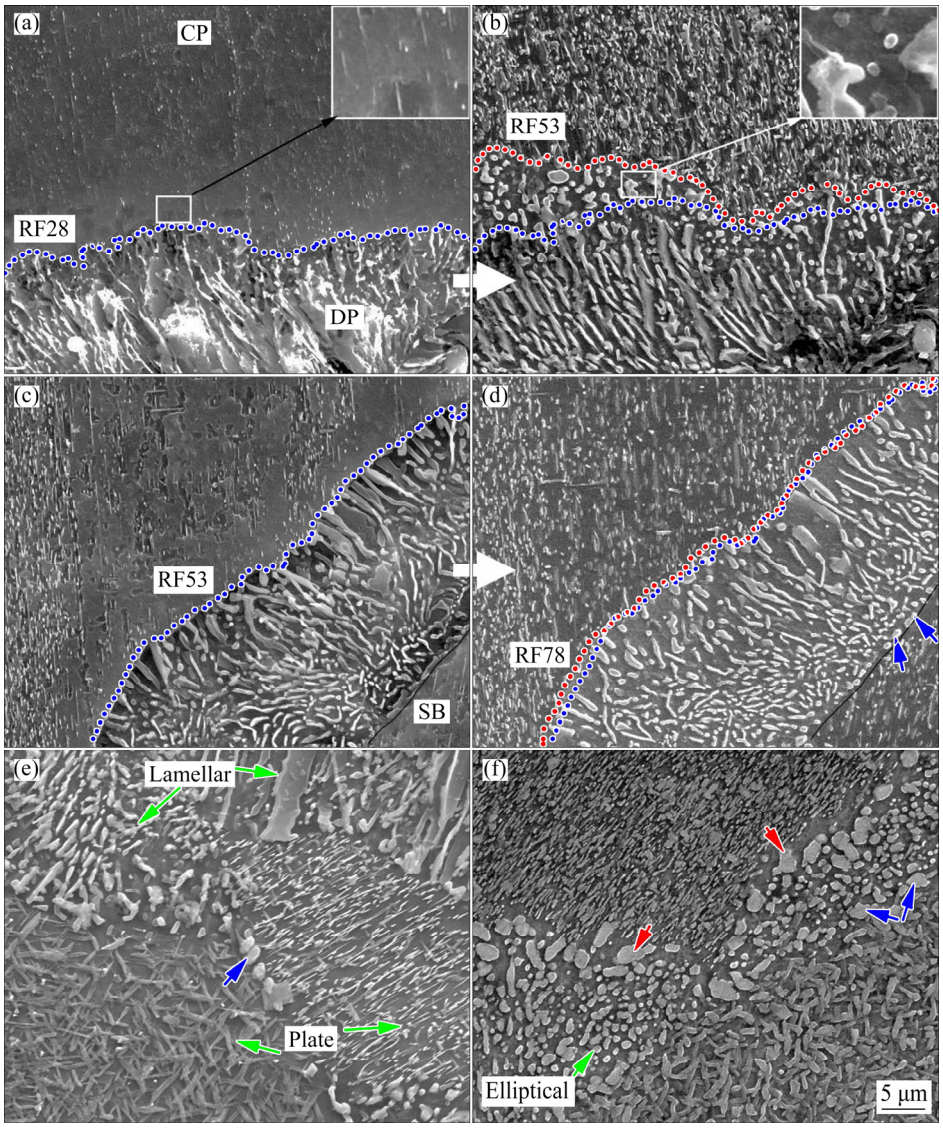

Fig. 4 SEM images of AZ80A magnesium alloy aged for different time: (a) 28 h; (c) 53 h; (e) 106 h; (f) 328 h; (b, d) In situ microstructures of sample at 28 h (a) and sample at 53 h (c) after further aging for 25 h, respectively

known as intergranular phases, and they grow continuously with increasing aging time, as shown in Figs. 4(d−f).

The precipitates in cellular structures are mainly lamellar phases and elliptical phases. The length direction of the lamellar phases and the long axis of the elliptical phases, as marked with blue double-arrow lines in Figs. 5(a) and (b), respectively, are randomly distributed in the α-Mg matrix, which is consistent with the research of LIU et al [24].

Figure 6 shows the high-magnification SEM images of lamellar phases in DP regions. With increasing aging time, no obvious coarsening occurs in the lamellar phases.

Figure 7(a) shows that the elliptical phases are small and dense at 28 h. However, they gradually become coarser with increasing aging time, as shown in Figs. 7(b−d) and Fig. 4(f) especially for those marked with red arrows.

3.2.3 Variation of microstructures in CP regions

It is also found in Figs. 4(e) and (f) that most of the precipitates in one CP region/original matrix grain are uniform but display different morphologies in different CP regions/original matrix grains, such as large bamboo leaf-like precipitates and needle-like precipitates. Figure 8 shows the high magnification SEM images of the needle-like precipitates. The precipitates are elongated with increasing aging time and do not stop until 106 h, as shown in Figs. 8(a−c). Its cross-section coarsens at 328 h, as shown in Fig. 8(d).

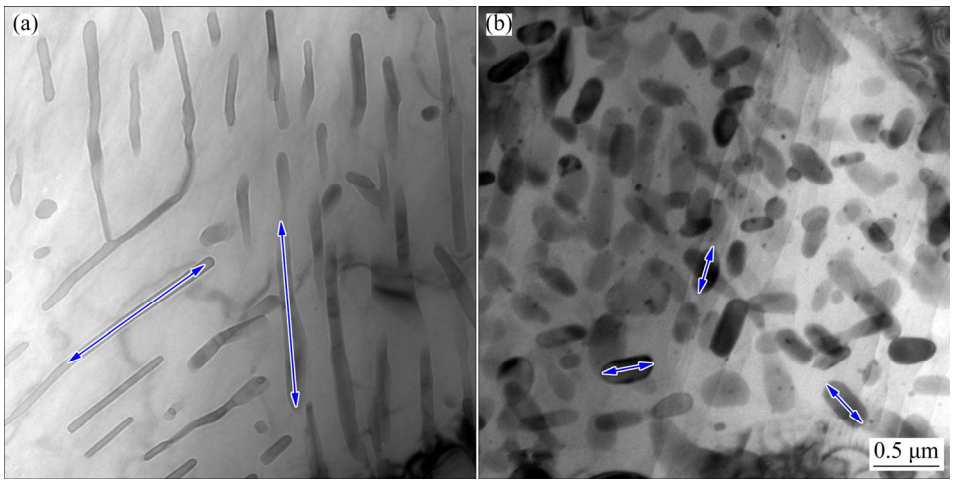

Fig. 5 TEM images of lamellar (a) and elliptical (b) phases

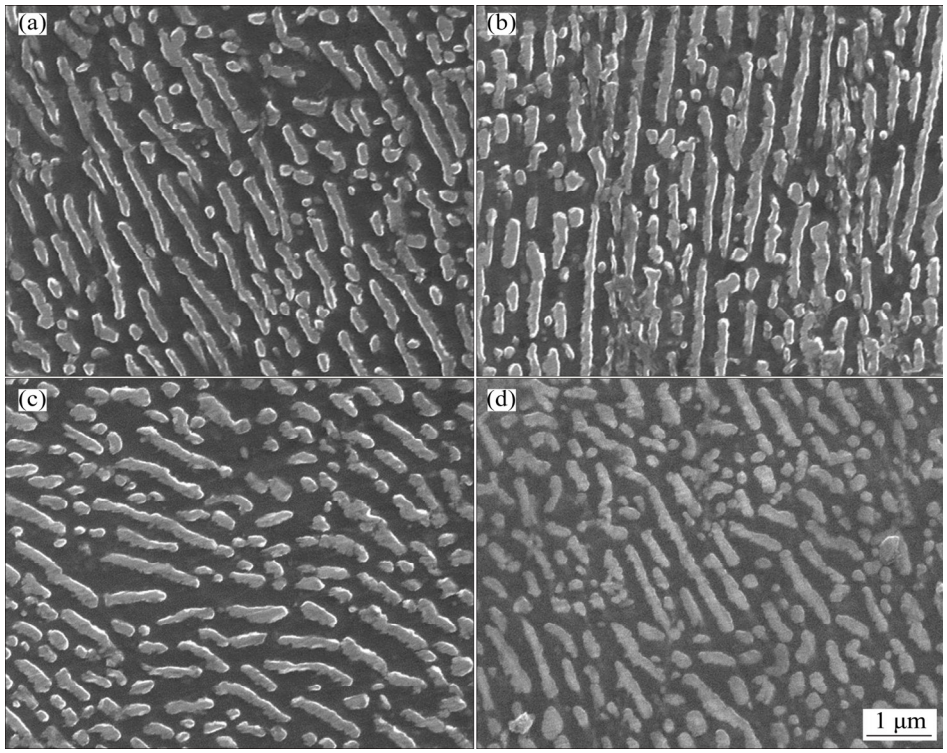

Fig. 6 High magnification SEM images of lamellar structures at aging time of 28 h (a), 53 h (b), 106 h (c) and 328 h (d)

The TEM images of precipitates in the CP regions are shown in Fig. 9. In view of the $[0001]_m$ zone axis, most precipitates exhibit asymmetric lozenge shapes (bamboo-leaf shape), and a few precipitates are irregularly hexagon-shaped (marked with red arrows), as shown in Figs. 9(a−c). Figures 9(d−f) show from the $[10\bar{1}0]_m$ zone axis that the majority of precipitates are thin and long needle-like phases with the length direction parallel to the $(0001)_m$ basal plane, and only a few lath phases (marked with red arrows) are perpendicular to the $(0001)_m$ basal plane. In addition, a few bulky phases (marked with blue arrows) are rectangularly shaped, and their length directions are parallel to the basal plane, as shown in Figs. 9(a, d). This indicates that the precipitates in CP regions can be divided into three types: many thin plate phases with a wide asymmetric lozenge shape on the basal plane, a small number of lath phases with irregular hexagonal cross-sections, and a few bulky phases with rectangular shapes. This explains why most precipitates in one CP region are uniform but display different morphologies in different CP regions.

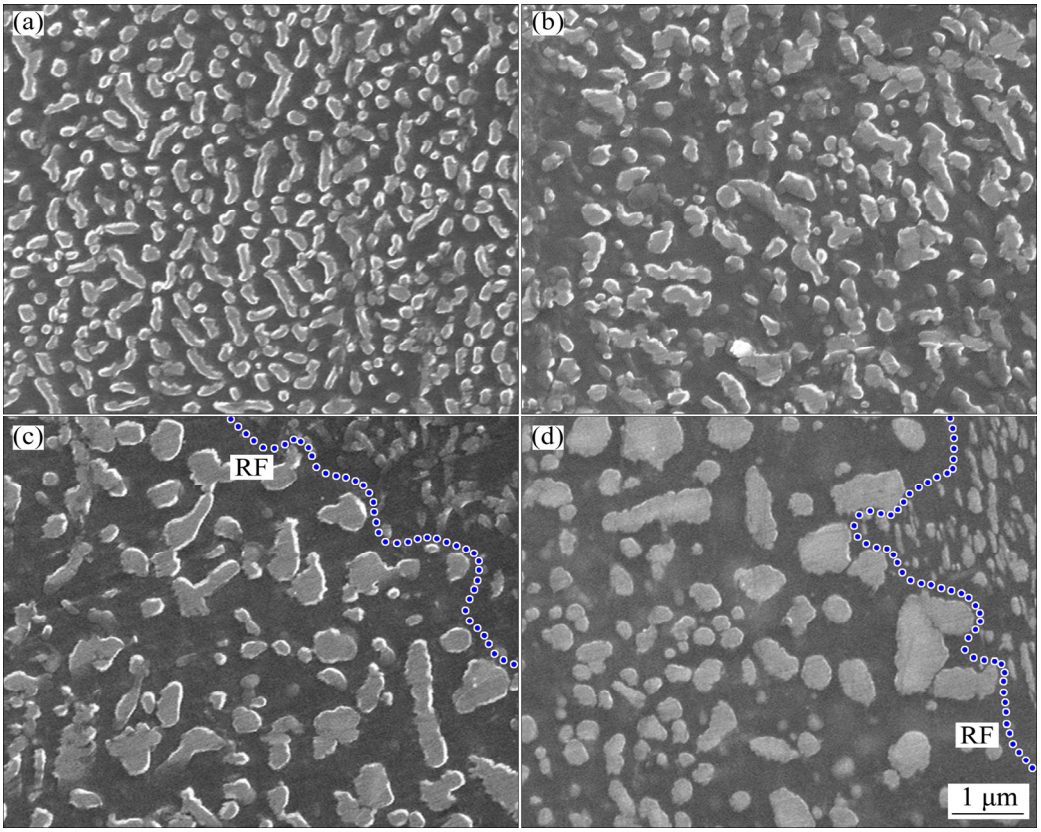

Fig. 7 High magnification SEM images of elliptical phases at aging time of 28 h (a), 53 h (b), 106 h (c) and 328 h (d)

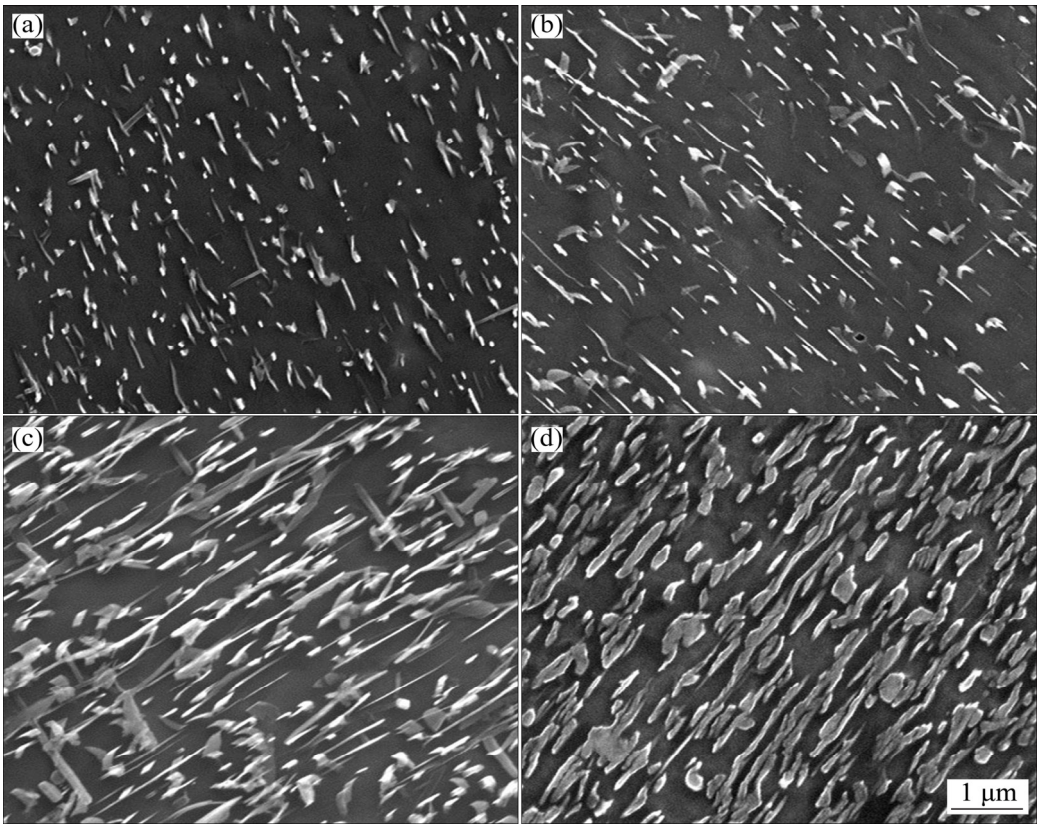

Fig. 8 High magnification SEM images of needle-line precipitates in CP regions at 28 h (a), 53 h (b), 106 h (c) and 328 h (d)

The plate and lath phases are reported in many articles [17−20], but the bulky phases are seldom reported. Figure 10(a) shows that a bulky phase with a short rectangular shape coexists with some thin plate phases, and the bulky phase is several times thicker than the plate phases. The HRTEM image of the bulky phase, as shown in Fig. 10(b), reveals that the $[11\bar{2}0]$ α-Mg orientation is parallel to the [111] β-$Mg_{17}Al_{12}$ and that the angle between [0001] α-Mg and [110] β-$Mg_{17}Al_{12}$ is 1.28°.

Small plate precipitates grow fast in length, width and thickness with increasing aging time, as shown in Figs. 9(a−c) and (d−f). Detailed data are measured from the TEM images and displayed in Table 1. At 28 h, the length, width and thickness reach 204.6, 84.2 and 23.0 nm, respectively. Subsequently, the plate phases grow slowly in length and thickness but still fast in width, as shown in Figs. 9(b, e). However, after aging for 328 h, the plate phases only grow in thickness, as shown in

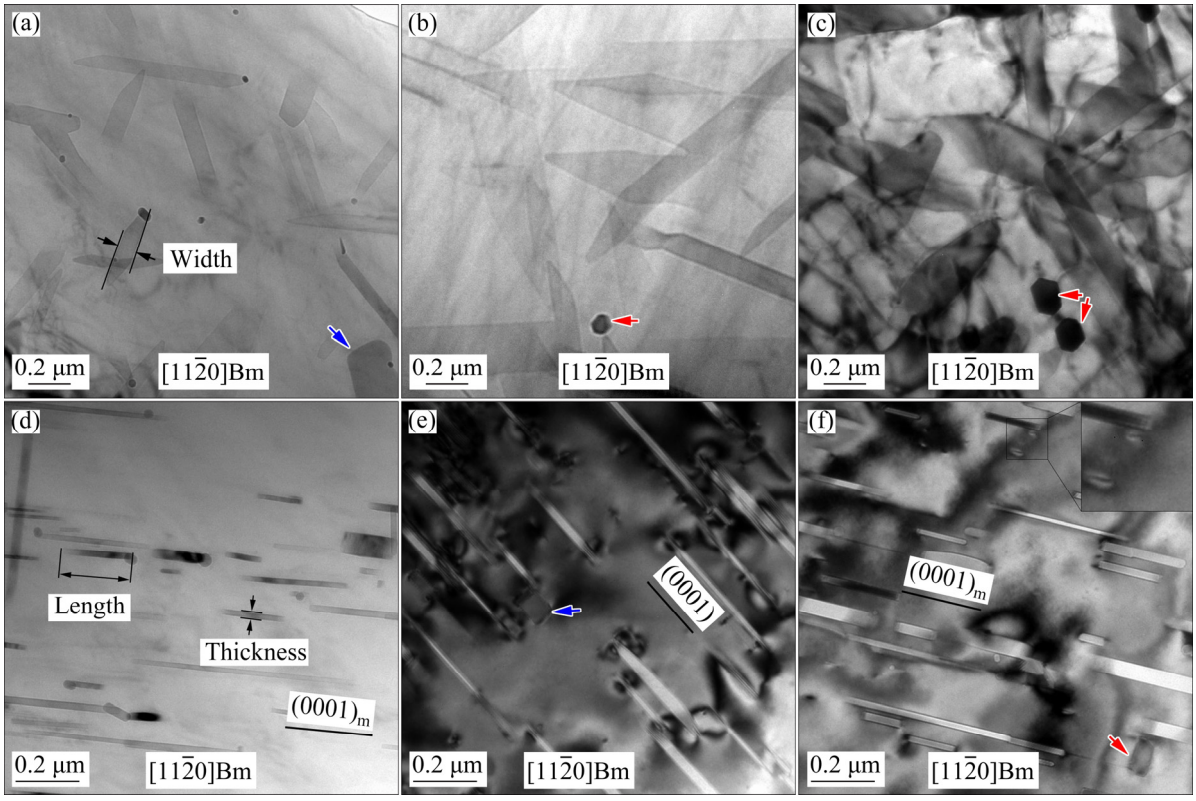

Fig. 9 TEM imagees of precipitates in CP regions at 28 h (a, d), 106 h (b, e) and 328 h (c, f)

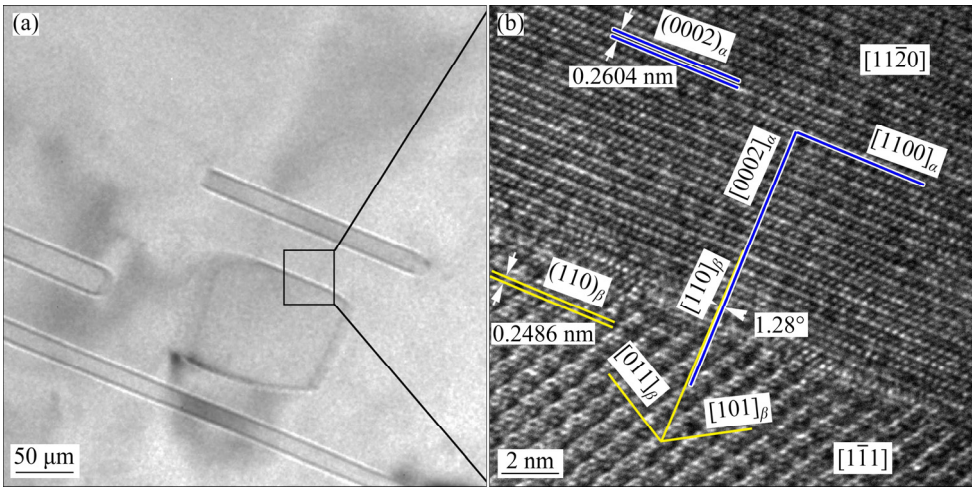

Fig. 10 TEM image of rectangular bulky phase (a) and its HRTEM image with α-Mg matrix along $[11\bar{2}0]$ α-Mg//[1$\bar{1}$1] β-$Mg_{17}Al_{12}$ direction (b)

Table 1 General dimensions of plate phases at different aging time

Aging time/h	Average length, *L*/nm	Average width, *W*/nm	Average thickness, *T*/nm
28	204.6±82.5	84.2±22.6	23.0±13.5
106	242.6±42.2	170.8±28.4	26.5±8.6
328	235.0±37.3	167.0±32.1	32.4±15.8

Fig. 8(d) and Figs. 9(c, f). Meanwhile, the amplified region in Fig. 9(f) shows a few tiny plate phases that have not been found before. In addition, apparent coarsening of the lath phases on the cross-section occurs when the aging time increases from 106 to 328 h. Evidently, the precipitation process of CP is much slower than that of DP.

3.3 Mechanical properties

The intracrystalline hardness in the DP and CP regions over aging time is shown in Fig. 11. With increasing aging time, the intracrystalline hardness of CP regions increases quickly at the beginning of the aging process and then slows down after 28 h, which is consistent with the hardness of the alloy described before. After 106 h, the intracrystalline hardness of the CP regions maintains a further flattened increasing trend. Different from the CP region, the hardness of the DP region maintains a very slow downward trend during the aging process. In addition, the intracrystalline hardness of DP regions is higher than that of CP regions during the whole aging regime carried out in this experiment.

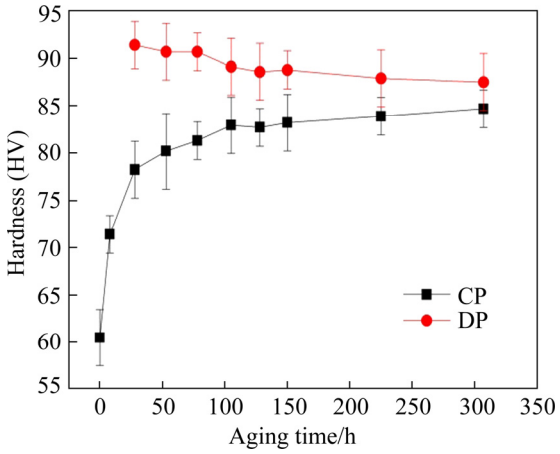

Fig. 11 Intracrystalline hardness of precipitates in DP and CP regions at different aging time

The tensile mechanical properties of the AZ80A magnesium alloy are shown in Table 2. At the beginning, the yield strength and tensile strength of the solution heat-treated alloy are 150 and 286 MPa respectively, and the elongation reaches 12.6%. With increasing aging time, both the yield strength and tensile strength are obviously improved before 106 h, and the increase in strength tends to be flattened at 328 h, but the elongation decreases continuously with increasing aging time. There is no overaging phenomenon in the regime of the aging time carried out in this experiment, and aging for 106 h at 175 °C is relatively suitable for the engineering application of AZ80A alloy.

Table 2 Tensile mechanical properties of AZ80A alloy at different aging time

Aging time/h	Yield strength/MPa	Tensile strength/MPa	Elongation/%
0	150±2	286±3	12.6±1.8
6	168±3	280±4	11.0±1.4
28	179±2	292±2	9.6±2.0
53	192±3	295±3	7.7±1.2
106	213±3	324±3	6.6±1.3
328	217±2	328±3	5.4±2.0

4 Discussion

4.1 Microstructure evolution

4.1.1 Microstructure evolution of DP regions

During discontinuous precipitation, the cellular structures originate from the grain boundary with a high misorientation angle, and then the RF of the cellular structures migrates toward the original matrix grains [23,25]. When the RF migrates through a specific undecomposed region, the DP reaction is so fast that the precipitation of this specific region is completed immediately (including the nucleation and growth of lamellar phases or elliptical phases), and the intracrystalline hardness reaches the peak value at once [18] because DP is controlled by grain boundary diffusion and the coefficient of boundary diffusion is much higher than that of other diffusion methods [16].

At the early aging stage, the precipitates of the CP region in front of RF are small and replaced by elliptical phases or lamellar phases with the aging time prolonging, which is different from the coexistence of the zinc-rich precipitation phase and lamellar phase in Ref. [26]. For the case in this

research, it is reasonable to infer that the fine precipitates in the CP region are transformed into elliptical or lamellar phases. In this reaction system, the driving force for the migration of RF is considered to be the decrease in the system free energy. When the precipitates in the CP region grow with increasing aging time, the driving force decreases due to the decrease in supersaturation of the original matrix. Once the driving force is too low, the RF stops migrating, and the cellular structure stops growing.

The LSW (Lifshitz−Slyozov−Wagner) theory can be used to describe the coarsening process of elliptical precipitates [27,28]. The kinetic equation for a spherical precipitate particle can be expressed as follows [29]:

$$r^3 - r_0^3 = \frac{8}{9}\frac{\Gamma C_e V_m^2 D}{KT}t \quad (1)$$

where r is the average radius of the growing particles at time t, r_0 is the radius at the beginning of the coarsening process, Γ is the interfacial free energy at the particle/matrix interface, D is the diffusion coefficient of solute atoms in the matrix, C_e is the concentration of solute atoms in equilibrium with a particle of infinite radius, K is the Boltzmann constant, T is the temperature of aging heat treatment, and V_m is the molar volume of precipitates. With increasing aging time t, larger particles become larger, and smaller particles gradually disappear with the diffusion of the solute atoms in the matrix. Thus, the number density of particles decreases during the coarsening process. Owing to the depleted α-Mg matrix in DP regions [18], the volume fraction of β-$Mg_{17}Al_{12}$ precipitates will no longer increase. Therefore, the edge-to-edge distance between precipitates logically increases with the coarsening of the precipitates, as shown in Fig. 7.

Because β-$Mg_{17}Al_{12}$ precipitates are incoherent with the α-Mg matrix and too large in size, precipitation strengthening is generally explained by the Orowan dislocation looping mechanism [30]. According to Orowan mechanism [31,32]:

$$\Delta\tau = \frac{Gb}{2\pi\lambda'\sqrt{1-\nu}}\ln\frac{d_p}{r_0'} \quad (2)$$

where $\Delta\tau$ is the increment in critical resolved shear stress, G is the shear modulus of the magnesium matrix phase, b is the magnitude of the Burgers vector of the dislocations, ν is Poisson's ratio, λ' is the effective planar interobstacle spacing, d_p is the mean planar diameter of the point obstacles, and r_0' is the core radius of dislocations. With increasing aging time, the coarsening of elliptical precipitates leads to an increase in the interparticle spacing λ' and ultimately a decrease in the critical resolved shear stress $\Delta\tau$. Therefore, the continuous decrease in intracrystalline hardness in DP regions is probably attributed to the coarsening of the elliptical phase.

4.1.2 Microstructure evolution of CP regions

After DP regions stop growing, the remaining original matrix regions tend to develop into CP regions. Since the CP mechanism controlled by volume diffusion is much slower than the DP mechanism controlled by the grain boundary diffusion [16], the precipitation process of plate phases in CP regions, including nucleation, growth and coarsening, is much slower than that of lamellar and elliptical phases in DP regions. Therefore, the nucleation and growth of plate phases occur, but the coarsening phenomenon is too late to appear in the entire aging regime of this research.

The increments in the size of plate phases and intracrystalline hardness of the CP region at different aging stages are obtained from Table 1 and Fig. 11, respectively. The plate phases grow very fast before 28 h, leading to large increments in size and the intracrystalline hardness of the CP region, as shown in Fig. 12. The increment in width (ΔW) increases at 106 h but that of the intracrystalline hardness (ΔH_{CP}) drops considerably, indicating that the width is unrelated to the hardness. At 28 and 106 h, the increments in length (ΔL) and thickness (ΔT_1) change consistently with those in ΔH_{CP}. ΔL stops increasing and ΔT increases slightly at 328 h, but ΔH_{CP} decreases continuously. However, the variation of the increment in the narrow section area (ΔS_{NS}) of the plate phases, which is determined by L and T_1, is highly consistent with that of ΔH_{CP} during the whole aging process. This suggests that the intracrystalline hardness of the CP region depends on the narrow section of the plate phases. It is well known that only the basal slip of the α-Mg matrix can be activated at room temperature [33]. Moreover, the narrow section is most effective in hindering basal slipping because it is perpendicular to the basal plane of the α-Mg matrix. Therefore, it is not difficult to understand why the variation

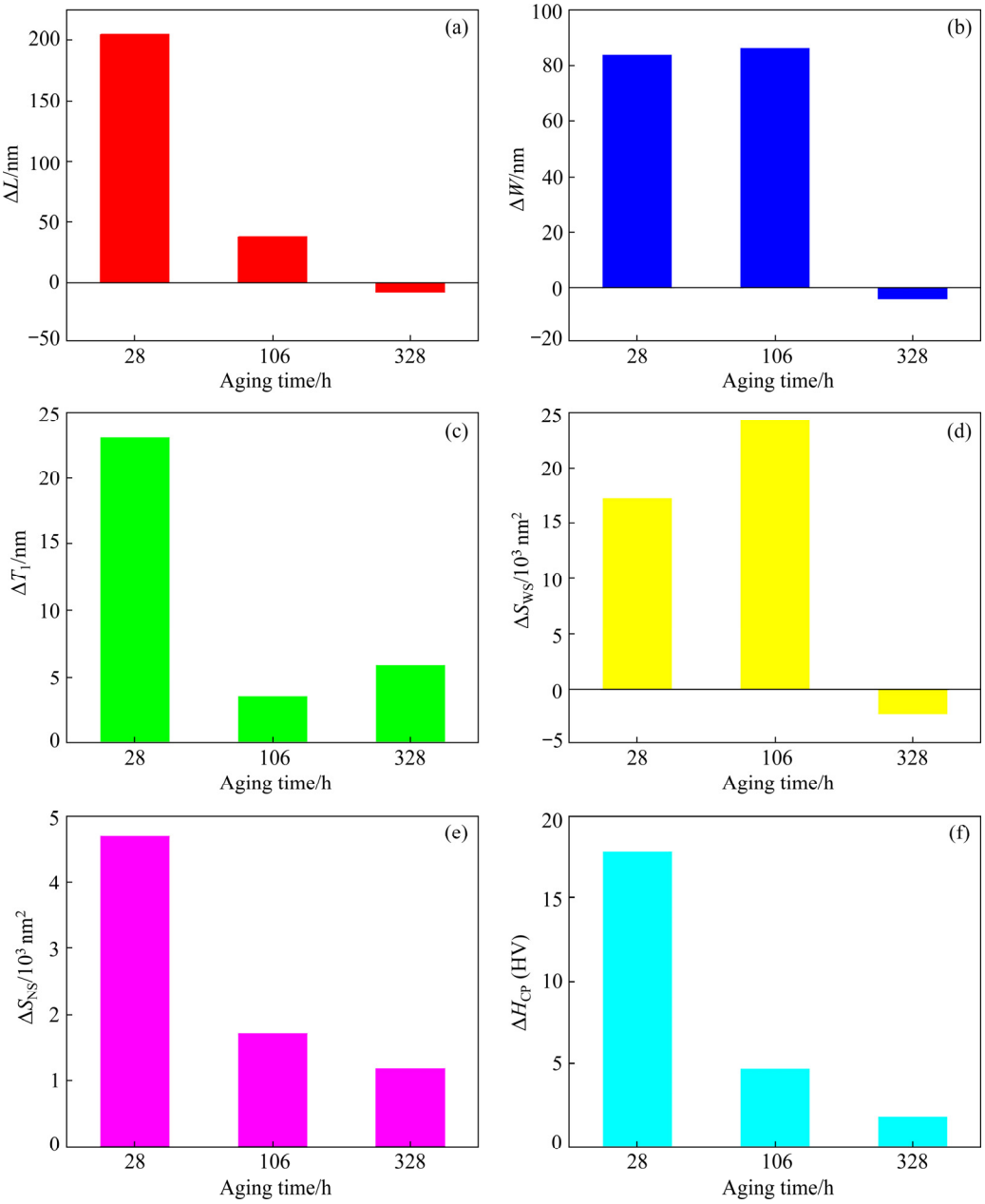

Fig. 12 Increments in length ΔL (a), width ΔW (b), thickness ΔT_1 (c), wide section area ΔS_{WS} (d) and narrow section area ΔS_{NS} (e) of plate phases and that of intracrystalline hardness of CP regions ΔH_{CP} (f) at aging time of 28, 106 and 328 h

of increment in the wide section area (ΔS_{WS}) of the plate phases, which is parallel to the basal plane of the α-Mg matrix and determined by length and width, deviates from that of ΔH_{CP}.

The rapid increase in the intracrystalline hardness of the CP region before 28 h is attributed to the nucleation of the plate phases and fast growth in length and thickness. In addition, the rectangular phases also work because they reach the maximum thickness. With increasing aging time, the growth of the plate phases in length and thickness slows down, which leads to the retardation of age hardening of CP regions. After 106 h, only the thickness still increases slowly, and some new small plate phases are formed simultaneously, which contributes to decreasing the interparticle spacing λ' and increasing $\Delta\tau$. Therefore, the intracrystalline hardness of the CP region remains in a slightly increasing trend rather than decreasing as that in the DP region due to overaging.

4.2 Comparison of age hardening effect between DP and CP regions

It is well known that the shape and orientation of the second phase are critical for strengthening the matrix [34]. For magnesium alloys, only three basal slip systems can be activated during deformation at room temperature [33]. Theoretically, any factor that has a negative impact on dislocation slipping is beneficial to the reinforcement of the matrix. As the main precipitation particles in CP regions, the narrow section of plate phases perpendicular to the basal plane is much smaller than the wide section parallel to the basal plane. As a result, the hindering effect of the particles on basal slip is weakened. However, in DP regions, the length direction of the lamellar phases and the long axis direction of elliptical phases are randomly arranged as mentioned above, which means that their largest cross-section is also randomly distributed. This leads to the fact that the lamellar and elliptical phases in DP regions are more likely to hinder dislocations on the basal plane than the plate phases in CP regions. Therefore, the strengthening effect of DP phase is better than that of CP phase. As a result, the intracrystalline hardness of DP regions is much higher than that of CP regions.

4.3 Effect of DP and CP on mechanical properties

When the AZ80A alloy is aged at 175 °C, the hardness of the alloy increases at a decelerating rate with increasing aging time. It increases rapidly at first, then decelerates obviously after 53 h, and finally reaches the peak value at 106 h, which is followed by no apparent changes. According to the rule of mixtures, the hardness of the alloy (H_{tot}) can be expressed as follows [15,16]:

$$H_{tot}=f_{DP}H_{DP}+f_{CP}H_{CP} \quad (3)$$

where f_{DP} and f_{CP} are the area fractions of DP and CP regions, respectively; H_{DP} and H_{CP} are the measured hardnesses of DP and CP regions, respectively; $f_{DP}H_{DP}$ and $f_{CP}H_{CP}$ are contributions of CP and DP regions to the hardness of the alloy, respectively. Figure 13 shows the contributions of the DP and CP regions to the hardness of the alloy. When the alloy is aged for 28 h at 175 °C, f_{DP} is approximately 43%, as shown in Fig. 1, and the other 57% is considered to be f_{CP}. In this case, $f_{DP}H_{DP} < f_{CP}H_{CP}$, i.e., the contribution of DP is smaller than that of CP, although H_{DP} is higher than H_{CP}, as shown in Fig. 11. At 53 h, f_{DP} increases to 58% by replacing parts of f_{CP}, so $f_{DP}H_{DP}$ increases quickly and dominates in strengthening the alloy. At flowing aging time, such as 106 and 328 h, f_{DP} and f_{CP} no longer change. $f_{DP}H_{DP}$ decreases slowly due to decreasing H_{DP}, and $f_{CP}H_{CP}$ increases because of increasing H_{CP}. However, $f_{DP}H_{DP} > f_{CP}H_{CP}$, i.e., DP regions always play a more important role in strengthening the alloy because f_{DP} remains higher than f_{CP} and H_{DP} remains higher than H_{CP} despite their variation with increasing aging time.

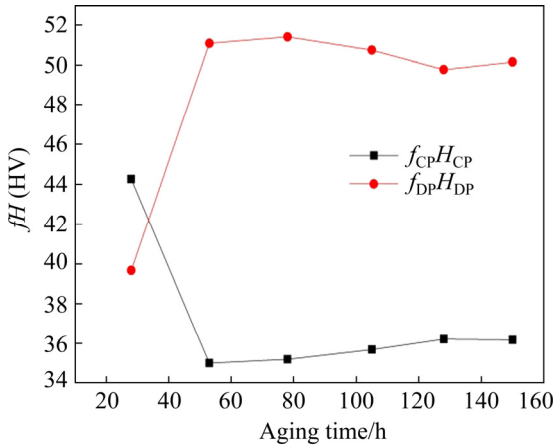

Fig. 13 Variation in contributions of CP and DP to alloy hardness over aging time

Even so, the increase in $f_{CP}H_{CP}$ induced by increasing H_{CP} not only compensates for the decrease in $f_{DP}H_{DP}$, but also makes H_{tot} increase between 53 and 106 h, which matches the increase in the alloy hardness in this period. After 106 h, the increase in H_{CP} further slows down. The increasing $f_{CP}H_{CP}$ just compensates for the decrease in $f_{DP}H_{DP}$. As a result, the alloy shows no obvious overaging phenomenon. Therefore, the CP regions also play a critical role in strengthening the alloy. If some measures are taken to accelerate the CP so that the peak aging point of CP is reached by the time when the DP region stops expanding, the alloy will obtain the optimum aging reinforcement.

5 Conclusions

(1) When the AZ80A magnesium alloy is aged at 175 °C, the precipitates in front of the RF are replaced by new elliptical phases or lamellar phases as the RF migrates with increasing aging time.

(2) CP is much slower than DP, leading to the

occurrence of the overaging phenomenon in the DP region and the absence of that in the CP region over the whole aging regime.

(3) In DP regions, the elliptical phases coarsen obviously with increasing aging time, which causes the intracrystalline hardness of DP regions to decrease.

(4) In CP regions, plate phases reach the maximum width and length at 106 h. Their thickness continues to increase during the subsequent aging process and some new small plate phases are reprecipitated, which is beneficial to a further slight increase in the intracrystalline hardness in CP regions.

(5) When the alloy is aged at 175 °C, DP plays the most significant role in the age hardening behavior of the AZ80A alloy because both the intracrystalline hardness and fraction of DP regions are much higher than those of CP regions. However, CP can not only compensate for the decrease in the strengthening effect of DP caused by overaging, but also improve the strength of the alloy.

Acknowledgments

This work was financially supported by the Natural Science Foundation of Hunan Province, China (No. 2018JJ2503), and the Postgraduate Independent Exploration and Innovation Project of Central South University, China (No. 1053320171111).

References

[1] ABDULLAEV R N, KHAIRULIN R A, KOZLOVSKII Y M, AGAZHANOV A S, STANKUS S V. Density of magnesium and magnesium−lithium alloys in solid and liquid states [J]. Transactions of Nonferrous Metals Society of China, 2019, 29: 507−514.

[2] HAN J G, JUN J H. Relationship between age-hardening by continuous precipitation and damping capacity in AZ91 alloy [J]. Materials Science and Technology, 2020, 36: 375−379.

[3] SUN Y H, WANG R C, PENG C Q, FENG Y, YANG M. Corrosion behavior and surface treatment of superlight Mg−Li alloys [J]. Transactions of Nonferrous Metals Society of China, 2017, 27: 1455−1475.

[4] FU P H, WANG N Q, LIAO H G, XU W Y, FENG L M, CHEN J, HU G Q, DING W J. Microstructure and mechanical properties of high strength Mg−15Gd−1Zn−0.4Zr alloy additive-manufactured by selective laser melting process [J]. Transactions of Nonferrous Metals Society of China, 2021, 31: 1969−1978.

[5] DZIUBIŃSKA A, GONTARZ A, DZIUBIŃSKI M, BARSZCZ M. The forming of magnesium alloy forgings for aircraft and automotive applications [J]. Advances in Science and Technology Research Journal, 2016, 10: 158−168.

[6] CHALISGAONKAR R. Insight in applications, manufacturing and corrosion behaviour of magnesium and its alloys—A review [J]. Materials Today: Proceedings, 2020, 26: 1060−1071.

[7] LI H Z, WEI X Y, OUYANG J, JIANG J, LI Y. Hot deformation behavior of extruded AZ80 magnesium alloy [J]. Transactions of Nonferrous Metals Society of China, 2013, 23: 3180−3185.

[8] DENG M, LI H Z, TANG S N, LIAO H J, LIANG X P, LIU R M. Effect of heat treatment on fracture toughness of as-forged AZ80 magnesium alloy [J]. Journal of Materials Engineering and Performance, 2015, 24: 1953−1960.

[9] NAKATA T, MEZAKI T, AJIMA R, XU C, OH-ISHI K, SHIMIZU K, HANAKI S, SASAKI T T, HONO K, KAMADO S. High-speed extrusion of heat-treatable Mg−Al−Ca−Mn dilute alloy [J]. Scripta Materialia, 2015, 101: 28−31.

[10] WANG Q, ZHANG Z M, ZHANG X, YU J M. Precision forging technologies for magnesium alloy bracket and wheel [J]. Transactions of Nonferrous Metals Society of China, 2008, 18(S): s205−s208.

[11] KULEKCI M K. Magnesium and its alloys applications in automotive industry [J]. The International Journal of Advanced Manufacturing Technology, 2008, 39: 851−865.

[12] HIDALGO-MANRIQUE P, ROBSON J D. Interaction between precipitate basal plates and tensile twins in magnesium alloys [J]. Metallurgical and Materials Transactions A, 2019, 50: 3855−3867.

[13] KIM S H, YOU B S, PARK S H. Effect of billet diameter on hot extrusion behavior of Mg−Al−Zn alloys, and its influence on microstructure and mechanical properties [J]. Journal of Alloys and Compounds, 2017, 690: 417−423.

[14] ZHANG K L, LI H Z, LIANG X P, CHEN Z, WANG L. Discontinuous and continuous precipitation characteristics and mechanical properties of a AZ80A magnesium alloy at different aging temperatures [J]. Materials Characterization, 2020, 161: 110146.

[15] KIM S H, LEE J U, KIM Y J. Accelerated precipitation behavior of cast Mg−Al−Zn alloy by grain refinement [J]. Journal of Materials Science & Technology, 2018, 34: 265−276.

[16] KIM J K, OH S H, KIM K C, KIM D H. Effect of aging time and temperature on the aging behavior in Sn containing AZ91 alloy [J]. Metals and Materials International, 2017, 23: 308−312.

[17] MIAO J S, SUN W H, KLARNER A D, LUO A A. Interphase boundary segregation of silver and enhanced precipitation of $Mg_{17}Al_{12}$ Phase in a Mg−Al−Sn−Ag alloy [J]. Scripta Materialia, 2018, 154: 192−196.

[18] JUNG I C, KIM Y K, CHO T H, KIM D H. Suppression of discontinuous precipitation in AZ91 by addition of Sn [J]. Metals and Materials International, 2014, 20: 99−103.

[19] CHE B, LU L W, WU M Y, KANG W, TANG L Y, FANG D Q. Effect of pre-aging on microstructure and mechanical properties of wrought magnesium alloy [J]. Materials Reports, 2021, 35: 21249−21258.

[20] CELOTTO S. TEM study of continuous precipitation in

Mg−9wt.%Al−1wt.%Zn alloy [J]. Acta Materialia, 2000, 48: 1775−1787.
[21] LEE J U, KIM S H, KIM Y J, PARK S H. Effects of homogenization time on aging behavior and mechanical properties of AZ91 alloy [J]. Materials Science and Engineering A, 2018, 714: 49−58.
[22] ROBSON J D. Modeling competitive continuous and discontinuous precipitation [J]. Acta Materialia, 2013, 61: 7781−7790.
[23] KESKAR N, PATTANAIK A K, MANI KRISHNA K V, SRIVASTAVA D, DEY G K. Kinetics and grain boundary selectivity of discontinuous precipitation in binary Ni−Cr alloy [J]. Metallurgical and Materials Transactions A, 2017, 48: 3096−3107.
[24] LIU C Q, LIU C L, CHEN H W, NIE J F. Heat-treatable Mg−9Al−6Sn−3Zn extrusion alloy [J]. Journal of Materials Science & Technology, 2018, 34: 284−290.
[25] LIU M J, SUN M, LI J H, CHEN L Y, DOU J N, WANG Y C, NI J M. Research progress on discontinuous precipitation modification of Mg−Al alloy [J]. Nonferrous Metal Materials and Engineering, 2020, 41: 39−47.
[26] TASHIRO K, PURDY G R. In situ observations of chemically induced grain-boundary migration and discontinuous precipitation in the aluminum−zinc system [J]. Metallurgical Transactions A, 1989, 20: 1593−1600.
[27] PANDEY P, KASHYAP S, PALANISAMY D, SHARMA A, CHATTOPADHYAY K. On the high temperature coarsening kinetics of γ' precipitates in a high strength $Co_{37.6}Ni_{35.4}Al_{9.9}Mo_{4.9}Cr_{5.9}Ta_{2.8}Ti_{3.5}$ fcc-based high entropy alloy [J]. Acta Materialia, 2019, 177: 82−95.
[28] XU Y T, LI H, LOU D C, WANG C. Effects of alloying elements on microstructure and coarsening behavior of Co−8.8Al−9.8W superalloys [J]. The Chinese Journal of Nonferrous Metals, 2021, 31: 1505−1515. (in Chinese)
[29] ZHOU Y H, LIU Y C, ZHOU X S, LIU C X, YU J X, HUANG Y, LI H J, LI W Y. Precipitation and hot deformation behavior of austenitic heat-resistant steels: A review [J]. Journal of Materials Science & Technology, 2017, 33: 1448−1456.
[30] JIANG B, ZHANG D D, SUN C, LI N X, LIU Y B, CAO Z Y. Microstructure evolution and creep behavior of high-pressure die-cast Mg−9Al−1Zn−1Sr alloy [J]. Materials Science and Engineering A, 2019, 766: 138388.
[31] MONDET M, BARRAUD E, LEMONNIER S. Microstructure and mechanical properties of AZ91 magnesium alloy developed by spark plasma sintering [J]. Acta Materialia, 2016, 119: 55−67.
[32] WANG J, ZHANG H T, FU H D, XIE J X. Effect of Cr content on microstructure and properties of aged Cu−Cr−P alloys [J]. Transactions of Nonferrous Metals Society of China, 2021, 31: 232−242.
[33] DAI S, WANG F, WANG Z, LIU Z, MAO P L. Effect of Cu on microstructure, mechanical properties, and texture evolution of ZK60 alloy fabricated by hot extrusion-shearing process [J]. Transactions of Nonferrous Metals Society of China, 2020, 30: 1511−1523.
[34] SANTOS-GUEMES R, BELLON B, ESTEBAN-MANZANARES G, SEGURADO J, CAPOLUNGO L, LLORCA J. Multiscale modelling of precipitation hardening in Al−Cu alloys: Dislocation dynamics simulations and experimental validation [J]. Acta Materialia, 2020, 188: 475−485.

时效时间对 AZ80A 镁合金中不连续析出相、连续析出相和力学性能的影响

张克龙[1]，李慧中[1,2,3]，梁霄鹏[1,2,3]，陈 智[1]，赵梓轩[1]，陶 慧[1]，周雄文[4]

1. 中南大学 材料科学与工程学院，长沙 410083；
2. 中南大学 粉末冶金国家重点实验室，长沙 410083；
3. 中南大学 有色金属材料科学与工程教育部重点实验室，长沙 410083；
4. 中南大学 湘雅医院 口腔医学中心 口腔修复科，长沙 410008

摘 要：通过 SEM 原位观察、TEM 观察和拉伸试验，研究 AZ80A 镁合金中析出相和力学性能随时效时间的演变规律。结果表明，在时效初期，反应前沿附近由连续析出(CP)产生的析出相逐渐被由不连续析出(DP)产生的析出相所取代。随着时效时间的延长，DP 区中的椭圆相明显粗化，导致 DP 区的晶内硬度缓慢降低；而在 CP 区，初始析出片状相长大的同时，还析出一些细小的片状相，这使得 CP 区的晶内硬度在时效后期继续缓慢增加。与 CP 区相比，DP 区具有更快、更强的时效硬化行为。然而，CP 区的时效强化不仅可以弥补 DP 区的过时效软化，而且还能提高合金的强度。

关键词：时效强化；不连续析出；粗化；原位观察；力学性能；镁合金

(Edited by Wei-ping CHEN)